electronics

MDPI

Article

The Influence of Geometric Parameters for Training an Artificial Neural Network to Predict the Band Structure of 1-D Fishbone Photonic Crystal

Fu-Li Hsiao, Chien-Chung Chen, Chuan-Yu Chang, Yi-Chia Huang and Ying-Pin Tsai *

Institute of Photonics, National Changhua University of Education, Changhua 50007, Taiwan; fulihsiao@cc.ncue.edu.tw (F.-L.H.); d1026001@mail.ncue.edu.tw (C.-C.C.); m1326002@mail.ncue.edu.tw (C.-Y.C.); d1226001@mail.ncue.edu.tw (Y.-C.H.)

* Correspondence: yingpintsai@gmail.com

Abstract: With the rising demand for the transmission of large amounts of information over long distances, the development of integrated light circuits is the key to improving this technology, and silicon photonics have been developed with low absorption in the near-infrared range and with sophisticated fabrication techniques. To build devices that work in different functionalities, photonic crystals are one of the most used structures due to their ability to manipulate light. The investigation of photonic crystals requires the calculation of photonic band structures and is usually time-consuming work. To reduce the time spent on calculations, a trained ANN is introduced in this study to directly predict the band structures using only a minimal amount of pre-calculated band structure data. A well-used 1-D fishbone-like photonic crystal in the form of a nanobeam is used as the training target, and the influence of adjusting the geometric parameters is discussed, especially the lattice constant and the thickness of the nanobeam. To train the ANN with very few band structures, each of the mode points in the band structure is considered as a single datapoint to increase the amount of training data. The datasets are composed of various raw band structure data. The optimized ANN is introduced at the end of this manuscript.

Keywords: silicon photonics; integrated light circuit; photonic crystal; fishbone-like nanobeam; photonic band structure; artificial neural network

check for updates

Citation: Hsiao, F.-L.; Chen, C.-C.; Chang, C.-Y.; Huang, Y.-C.; Tsai, Y.-P. The Influence of Geometric Parameters for Training an Artificial Neural Network to Predict the Band Structure of 1-D Fishbone Photonic Crystal. *Electronics* **2024**, *13*, 1285. https://doi.org/10.3390/electronics13071285

Academic Editor: Frédérique Ducroquet

Received: 28 February 2024
Revised: 27 March 2024
Accepted: 28 March 2024
Published: 29 March 2024

Copyright: © 2024 by the authors. Licensee MDPI, Basel, Switzerland. This article is an open access article distributed under the terms and conditions of the Creative Commons Attribution (CC BY) license (https://creativecommons.org/licenses/by/4.0/).

1. Introduction

In recent years, the development of integrated light circuits (ILCs) has been pushed by the demand for long-distance information transmission and the transmission of large amounts of data at a high speed. Currently, silicon is the most employed material in ILCs, not only due to its low absorption in the near-infrared range, but also the sophisticated fabrication process that is used to make semiconductor devices. The studies on these silicon-based photonic devices describe them as silicon photonics. To work as a traditional electric circuit, lots of devices with different functions are required for the ILC, including light sources [1–5], resonators [6–10], and sensors [11–15]. In various designs of devices for silicon photonics, photonic crystals (PtCs) are one of the commonly used structures for building circuit elements. The periodically arranged scatter elements give PtCs the ability to manipulate propagating light waves through a special dispersion relation, known as photonic band structures (PBSs). The PBSs are similar to electron energy band structures, which show the states of the electrons within semiconductors. The characteristics of PtCs can be observed from the corresponding PBSs and include the photonic forbidden band gap [16–20], negative refractive indices [21–23], or slow light [24–26]. Therefore, the study of PBSs is usually the first and most important step in PtC device design.

Typically, PtCs are composed of two or three different materials, including the surrounding background material and the host material, and sometimes, the scattering ele-

ments are composed of composite materials. According to the arrangement of the scatter elements, PtCs can be formed in one to three dimensions in space to manipulate light waves propagating in different directions. Considering the configurations of ILCs and their difficult fabrication, the most used PtCs are the 1-D and 2-D configurations, used as waveguides [27–29], resonators [30–32], and filters [33–35]. Based on the characteristics of forbidden band gaps, 2-D PtC structures can easily form waveguides or resonators by creating defect regions in the periodic surface. In contrast, when considering the large refractive index difference between the host and the background materials, such as silicon and air, 1-D PtCs can directly act as a waveguide and form filters or resonators with the PtC structure in a relatively small area. Similar to 2-D PtCs, resonators can be built with photonic band gaps. By drilling holes periodically in a nanobeam forming PtC structures, high-quality cavities can be made in the defect region with small sizes. Besides drilling holes, arranging pillars on the surface of the nanobeam is another way to form PtC structures. To simplify the fabrication process, these pillars are usually arranged on the side walls of the nanobeam and remain with the main waveguide in the same plane, producing a fishbone-like PtC structure [36–38]. This kind of PtC has the advantage of an acousto-optic structure, which is a result of its fishbone-like pillars [39–41], and due to this pillar-type structure, it can generate phononic band gaps much more easily than a hole-type structure could, producing high-quality acoustic resonators that can be combined with the photonic resonators perfectly.

Regarding PtCs configured in different dimensions, the reciprocal lattice space has different unit k-vector pairs; the corresponding PBSs are depicted with these unit k-vectors within the reduced Brillouin zone and illustrated in different configurations. The finite element method (FEM) is one of the most frequently used methods for calculating PBSs. By meshing a huge geometry into small elements, the FEM is good at solving structures with complex geometries. Through the periodic boundary conditions set according to Bloch's theory, FEM can actually calculate the PBSs by the unit cell of PtCs to reduce the calculation time. In order to fully understand the dispersion relation of a certain PtC structure, numerous PBSs need to be investigated. When the characteristics of a designed PtC operate in an unwanted frequency range, the geometric parameters of the PtC should be changed to fit the desired operation frequency. For this reason, lots of PBSs calculated in different geometric parameter combinations are required to discuss the relationship between the frequency shifts of each photonic mode within the PBS and the varying geometric parameters, which therefore causes a time-consuming problem.

In the past decade, research on artificial neural networks (ANNs) has attracted growing attention. Their powerful prediction and classification ability have led to great achievements in various fields and techniques, such as the convolution neural network (CNN), machine learning, and deep learning. Neural networks are good at dealing with repetitive but complex problems, such as pattern recognition [42–44], optical device design [45,46], or even biometric identification [47]. Solving the nonlinear relevance between the parameters and characteristics requires many repetitive calculations, which are very time-consuming. By pre-training a network for the specific problem, the nonlinear relevance can be hidden in the configuration and weights of the neural network and directly provide the desired result to users, saving time otherwise spent performing calculations.

In this study, the aim is to train an ANN to directly produce the PBS of a 1-D fishbone-like PtC with specified geometric parameters and to reduce the need for raw data for training, while maintaining accuracy. All the required PtC conditions were considered in the FEM simulations, and the simulated PBSs are treated as the training data for the ANN. Due to the guiding mechanism of the waveguide, the shape of the cross-section will affect the propagation conditions and change the PBS result significantly. Thus, most of the adjustments of the structure focus on the other parameters of the details' shapes, such as the radii of the drilled holes or the height of the pillars, and these parameters also become the main features used for ANN training. However, the effect of the cross-sectional parameters, like the thickness, still needs to be discussed to enable structure optimization. Furthermore,

the lattice constant is the most important parameter for PtC structures, representing the periodic length of the unit cell, and controls the operation wavelength range based on the scattering mechanism. The change in the lattice constants will directly affect the operation wavelength and shift the frequency of the photonic modes. Although the variation in the operation wavelength is proportional to the lattice constant to a certain extent, the relationship is not linear, and even some modes with high correlations with the lattice constant will shift independently.

In the following sections, the prediction results obtained with the trained ANN will be discussed in terms of several combinations of geometric parameters, especially for different lattice constants and different thicknesses, which affect PBSs the most. The raw PBS data calculated by the FEM will be separated into the training group and the testing group, where the former is used for training the ANN, and the latter is used to test the trained ANN for comparison.

2. Materials and Methods

The fishbone-like PtC is formed by drilling half-cylinder air holes on both sides of the nanobeam and adding additional wings on the remaining parts, as shown in Figure 1. The parameters are detailed in the sketch; the periodic length of the PtC and the thickness of the nanobeam are denoted as a and H; the width of the nanobeam, w, is defined as being equal to a; and, finally, the details of the fishbone shape, which are the radius of the air holes and the wing lengths, are defined as r and d. The raw PBS data are first calculated by the FEM, as mentioned in the introduction. The PtC structure is made of silicon and surrounded by air, and the refractive indices are set as 3.46 and 1, respectively. Regarding the parameters, a and H are treated as the main parameters and correspond to the same r and d pairs. For the sub-parameters, r and d, the magnitudes are defined by a ratio to a, where each group of a and H is defined as $r = 0.1a \sim 0.45a$ and $d = 0.1a \sim 1a$.

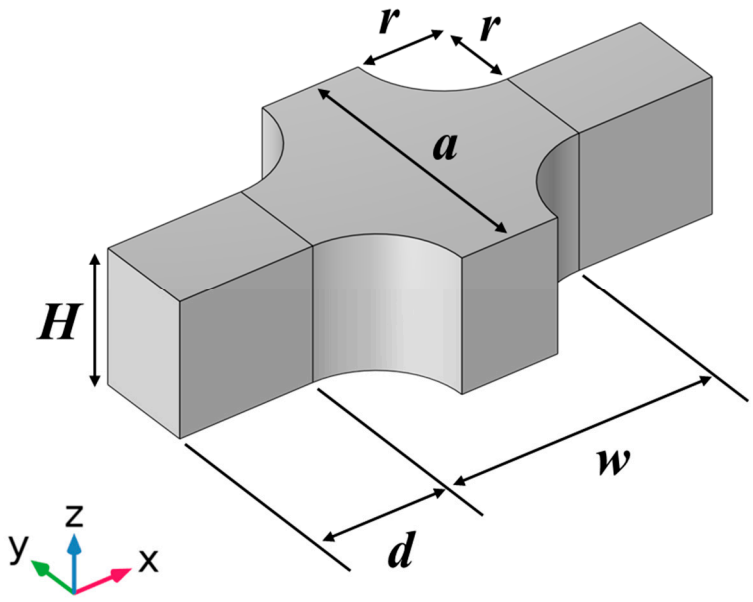

Figure 1. Sketch of the fishbone-like PtC structure.

For instance, Figure 2 illustrates six PBSs for PtCs with the same d and r pair both equal to $0.3a$, but different a and H to show the influence of the main parameters. It should be noted that only the five lowest solutions for the photonic band exist in the PBS, which maintains the band distribution's relative simplicity within the PBS. First, in Figure 2a–c, PBSs with the same a/H ratio are compared, where the magnitudes of a and H in the three PBSs are (a) a = 220 nm, H = 110 nm; (b) a = 440 nm, H = 220 nm; and (c) a = 880 nm, H = 440 nm. All three PBSs show the same mode configurations, and the frequency ranges shown in the y-axis are the only differences that can be observed, revealing that equally and

proportionally enlarging or reducing the size of the PtCs only affects the total frequency ranges of the final PBS. Second, in Figure 2a–f, PBSs with the same value of a but different values of H are compared in groups, where the parameters are (d) a = 220 nm, H = 220 nm; (e) a = 440 nm, H = 660 nm; and (f) a = 880 nm, H = 220 nm. When observing the three pairs of PBSs, the configurations are clearly changed but maintained in the same frequency range, concluding that adjusting H affects only the mode configurations. Finally, PBSs with the same value of H but different a values are compared in Figure 2b,d,f. Due to the setting of w, adjusting a also changes the width of the nanobeam at the same time and, therefore, affects not only the frequency ranges but also the configuration of the whole PBS.

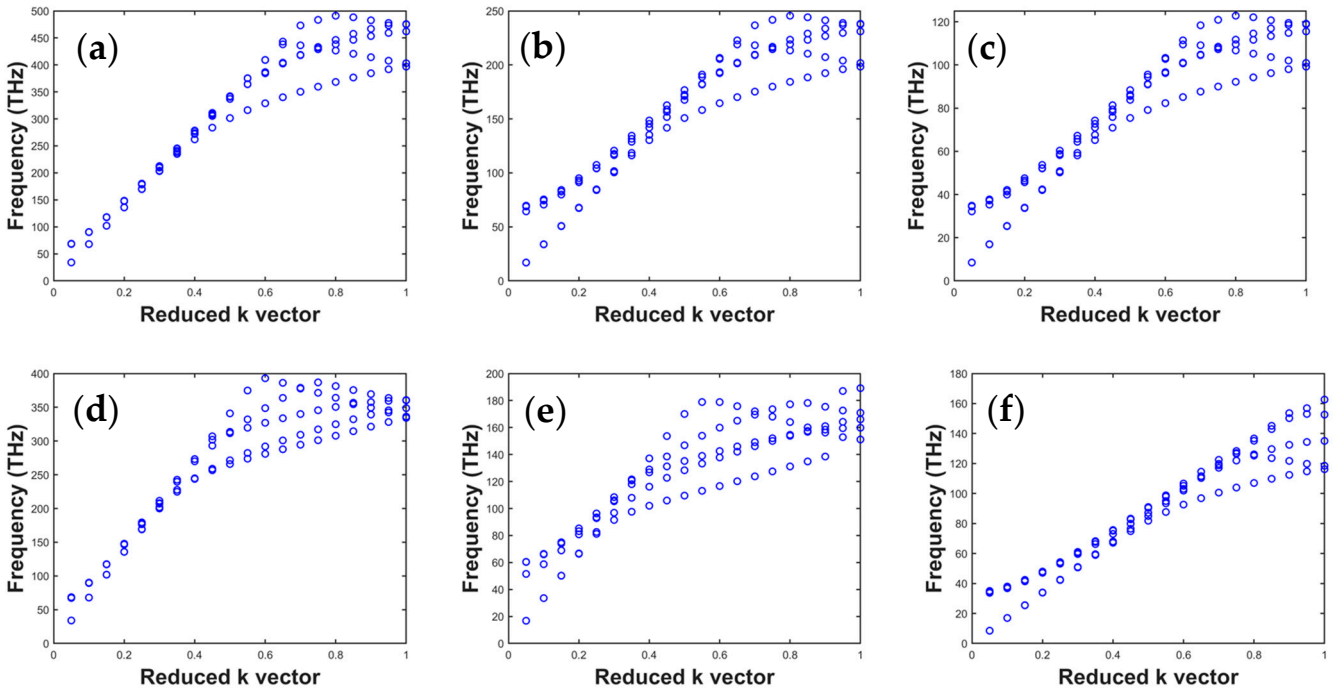

Figure 2. Photonic band structures of PtCs in which (**a**) a = 220 nm, H = 110 nm; (**b**) a = 440 nm, H = 220 nm; (**c**) a = 880 nm, H = 440 nm; (**d**) a = 220 nm, H = 220 nm; (**e**) a = 440 nm, H = 660 nm; and (**f**) a = 880 nm, H = 220 nm.

Regarding the ANN training configurations, the standard fishbone-like structure with a = 440 nm and H = 220 nm is first used as the testing target. To enlarge the data points for training, each point in the PBSs is considered as a single datapoint. The geometric variables, d and r, and the coordinate information of the mode points within the PBSs represented by the reduced k-vector and the eigen solution order (EO) are chosen as the training features, while the eigenfrequencies are the target solutions for prediction. Figure 3a shows the configuration sketch of the ANN for a standard fishbone PtC. The four neurons in the input layer represent the aforementioned features, and the one neuron in the output layer is for the target frequencies. In the hidden layer, two layers with 25 neurons are selected for training, marked as h_{mn} in the figure, where m represents the order of the hidden layer and n represents the order of the neuron; the software will automatically tune the weight of the hidden neurons during training. The ranges of d and r are $0.1a \sim 1a$ and $0.15a \sim 0.45a$ in increments of $0.1a$ and $0.05a$, respectively.

To further investigate the influence of adjusting a and H on ANN training, a similar ANN configuration with different input neurons is used, as shown in Figure 3b. Contributed by the additional features a and H, the increments of d and r can be increased twice before reducing the demand for the PBS's data numbers. The extended training datasets are separated into three groups, which change H while fixing a = 440 nm, change a while fixing H = 220 nm, and fix a/H = 2, named the a440 group, H220 group, and aH2 group,

respectively. Each training dataset group contains three pairs of main parameters and twenty pairs of sub-parameters, as shown in Table 1.

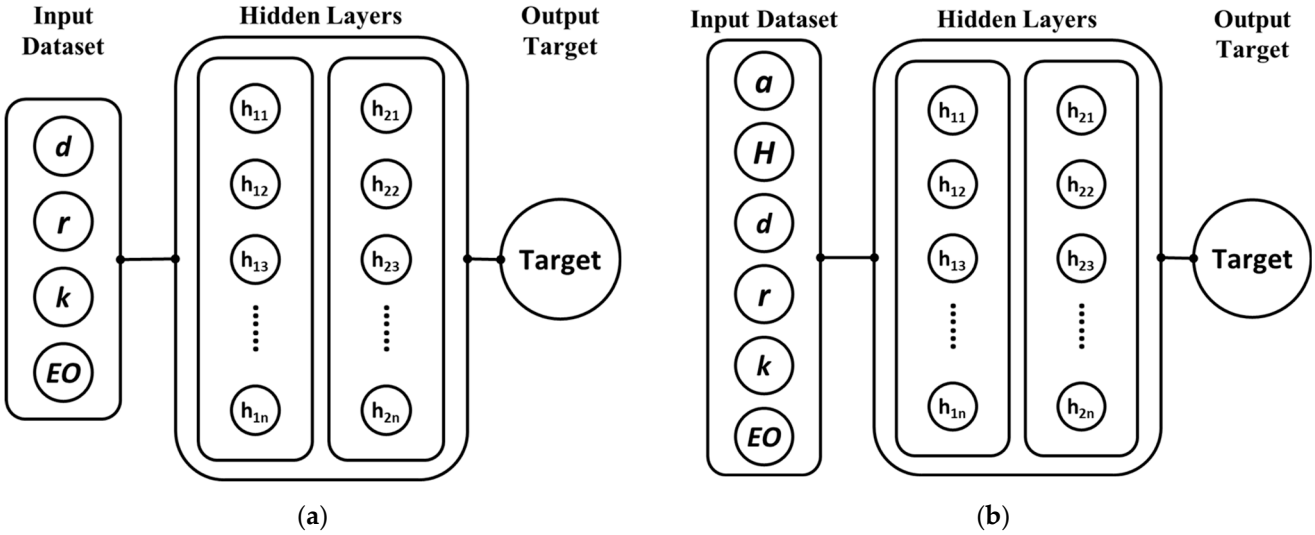

Figure 3. Configuration sketch of the ANN for (**a**) standard fishbone structure training and (**b**) adjusting *a* and *H* training.

Table 1. Three training datasets with different parameter combinations.

		a440	H220	aH2
Main parameters	*a*	440 (nm)	220/440/880	220/440/880
	H	220/440/660	220	110/220/440
Sub-parameters	*d*		0.2*a*, 0.5*a*, 0.8*a*	
	r		0.15*a*, 0.30*a* 0.45*a*	

3. Results

3.1. Standard Fishbone Structure Training

The PBSs of the standard fishbone PtCs are first calculated by the FEM using a PtC unit cell. The raw PBS data are then combined and reshaped according to the feature matrix for the ANN input layer and the target matrix for the output layer. During the training process, the training dataset is separated into three parts by a certain ratio (7:2:1 in this part) that can be defined as the training data, the validation data, and the testing data. Figure 4 illustrates the four PBSs calculated by the FEM (in the blue circle) and predicted by a trained ANN (in red points) for the standard fishbone PtC. To balance the complexity and the performance of the ANN, the prediction accuracy of the data that are and are not included in the training dataset is required for judgment, where the accuracy for the data included in the dataset represents the basic performance of the ANN, and the accuracy for those not included can show whether the net is overfitted or not. By calculating the linear regression for the predicted value and the target value, the slope of the regression line can be treated as the accuracy for the corresponding issue. According to the range of *d* and *r*, the PBS data of the PtC structure with $d = 0.1a$ and $r = 0.15a$, shown in Figure 4a, are contained in the training dataset and show great accuracy with a high regression coefficient R of 0.99997 and a training time of around 30 s, while a single FEM calculation needs around 120 s.

For a well-trained ANN, the prediction result of the data contained in the training dataset should naturally exhibit a high accuracy, so it still needs data that are not contained in the original training dataset to test the performance. In Figure 4b,c, the PBSs for the PtC structures with a *d* or *r* that is not contained in the training data list are shown by the blue circles and red points, and furthermore, in Figure 4d, the PBS for the structure with both

the *d* and *r* not contained in the training data list is shown. All three datasets belong to the data outside the training dataset. The highly matched results in Figure 4b–d confirm the prediction ability of the ANN for standard fishbone PtC structures.

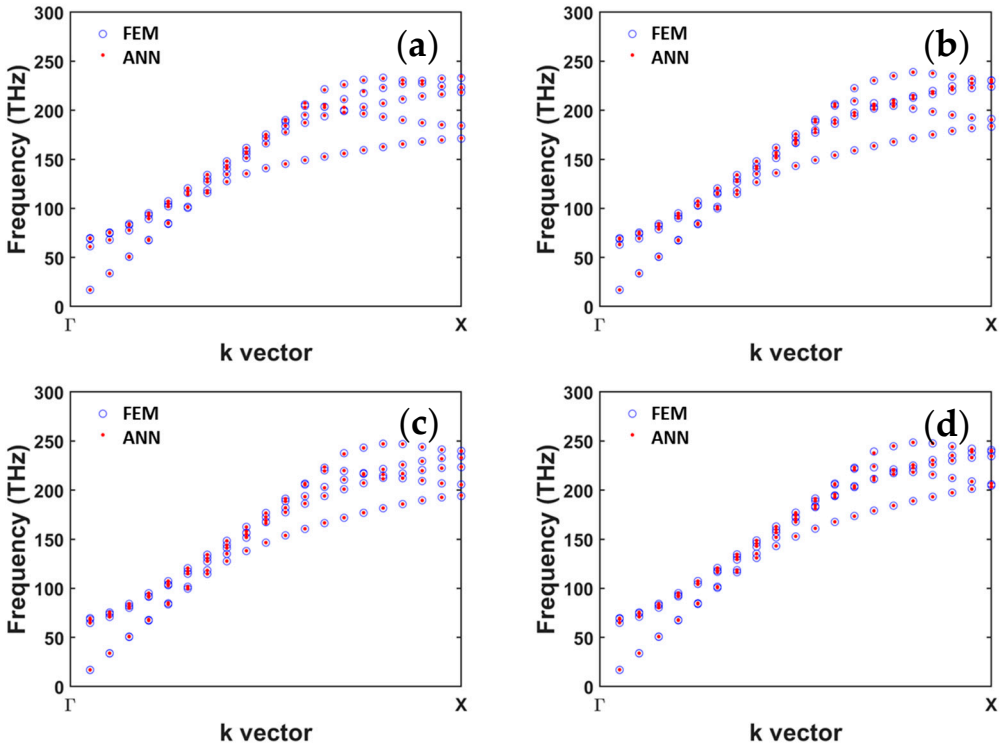

Figure 4. Prediction results (red points) compared with PBS raw data calculated by FEM (blue circles) of PtCs with a = 440 nm, H = 220 nm and (**a**) $d = 0.1a$, $r = 0.15a$; (**b**) $d = 0.32a$, $r = 0.25a$; (**c**) $d = 0.5a$, $r = 0.32a$; (**d**) $d = 0.32a$, $r = 0.32a$.

3.2. Adjusting a and H training

As mentioned in the second section, variables a and H provide additional combinations for the dataset, and the increments of d and r data can be increased during this training. To magnify the difference between the influence of the sub-parameters and the main parameters, the number of d and r values is reduced to the same as that of a and H, and therefore, the number of PBSs in each dataset is kept at $3 \times 3 \times 3$ =27. In Figure 5a–c, the prediction results of the three datasets a440, H220, and aH2 are represented by PBSs of the same structure with a = 440 nm, H = 220 nm, $d = 0.4a$, and $r = 0.2a$. As shown in Table 1, this parameter combination is not contained in the range of d and r, so the prediction results can represent the prediction ability for the sub-parameters under different main parameter conditions.

For the dataset a440, because a is fixed at 440 nm, the prediction result shows the influence of adjusting H. In Figure 5a, the prediction results shown by the red crosses fit well with the calculated results represented by the blue circles, showing that the prediction ability for the sub-parameters is still as effective as it was before adding the main parameters. However, in Figure 5d, the result of predicting the structure with H = 550 nm, which is not included in the H training list, shows some mismatching, pointed out by the arrows. Unlike adjusting the sub-parameters, which only slightly changes the PBS, adjusting H changes the configuration of the PBS on a larger scale even though the number of values of parameters in the training dataset is the same, meaning that even with the same amount of information for ANN training, the prediction result cannot maintain the accuracy for an untrained value of H.

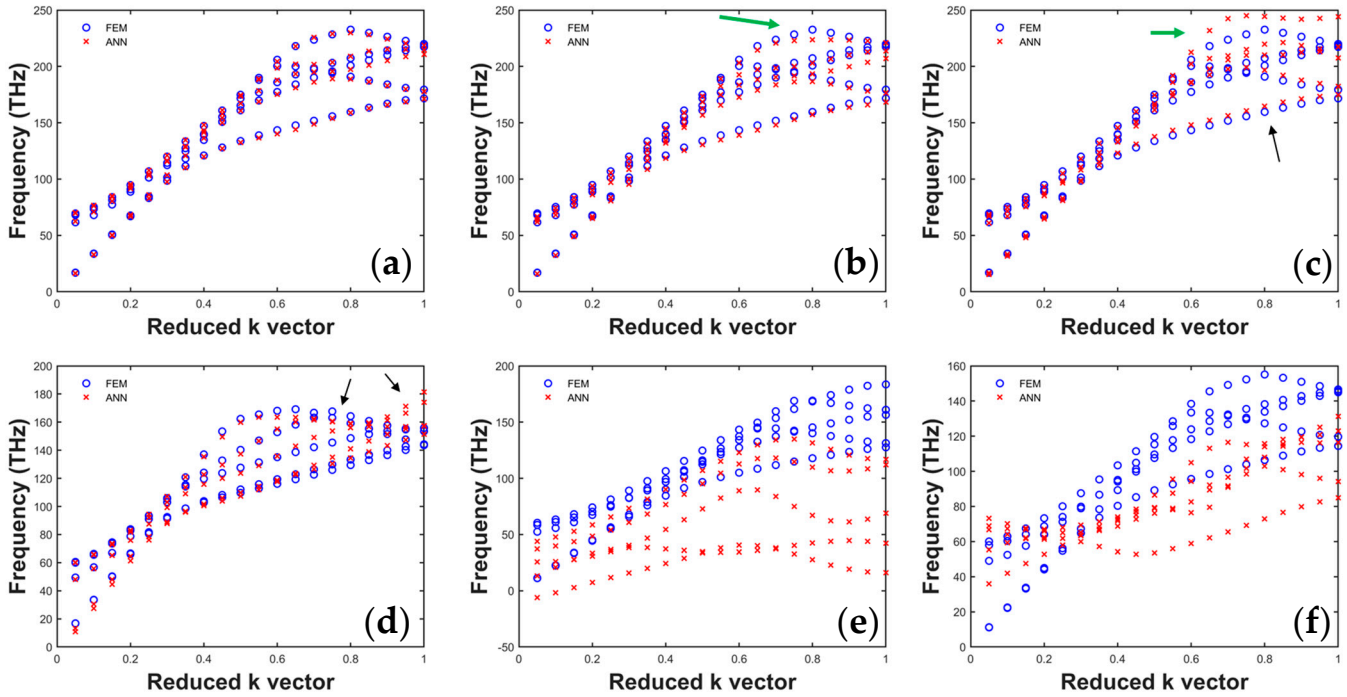

Figure 5. Prediction results (red x points) compared with PBS raw data calculated by FEM (blue circles) of PtCs with a = 440 nm, H = 220 nm, d = 0.4a, and r = 0.2a using (**a**) a440, (**b**) H220, and (**c**) aH2 datasets, and the prediction results for data not contained in the a and H training lists, where (**d**) a = 440 nm, H = 550 nm using the a440 dataset; (**e**) a = 660 nm, H = 220 nm using the H220 dataset; and (**f**) a = 660 nm, H = 330 nm using the aH2 dataset.

For the dataset H220, because H is fixed at 220 nm, the prediction result shows the influence of adjusting a. In Figure 5b, the prediction results represented by the red crosses fit less than in dataset a440. As pointed out by the green arrow, some points exhibit a little mismatch but are still within the allowable range. In Figure 5e, the result shows terrible mismatching in predicting the structure with a = 660 nm. As described in Figure 2, adjusting a will affect not only the configuration of the PBS but also the frequency range. Therefore, training with limited information causes mismatches in both the configuration and the frequency for most of the points.

Finally, the dataset aH2 fixes the a/H ratio and produces less change in the PBS configurations, but more in the frequency range. For the data in the a/H training list, Figure 5c maintains good prediction results but fits less than in H220. The data pointed out by the green arrow have a larger mismatch than in H220, and those pointed out by the black arrow also show worse fitting than in H220. In Figure 5f, the mismatch problem still exists in predicting the structure with parameters not included in the a/H training list. As described in Figure 2, adjusting a/H will only affect the frequency range and maintains the entire configuration of the PBS. The limited information then causes the mismatch of most of the points.

3.3. a and H training Optimization

The regression coefficients, R, of the ANN with the three datasets are 0.9996, 0.99982, and 0.99998 for the a440, H220, and aH2 datasets, respectively. All the values of R are over 0.999, and the aH2 dataset has the highest value while a440 has the lowest. Since the R value only reflects the degree of fitting between the prediction point and the target value, when the composition of the dataset is relatively simple, the fitting results can be expected to be better, but dealing with new data will be more difficult with an overly simple dataset. One of the solutions is to increase the amount of training data. However, increasing the demand for pre-calculated PBS data will make ANN prediction lose its purpose.

Since the problem that occurs during training is similar to that of overfitting, another solution for not increasing the raw PBS data is to adjust the training data separation ratio and the construction of the ANN. To optimize the training for the non-contained data, the separation ratio for the testing data is increased, and the final ratio becomes 70% training data, 10% validation data, and 20% testing data from the original ratio of 7:2:1. Regarding the construction of the ANN, the number of hidden layers is increased to three, and the numbers of neurons in the hidden layers are optimized to ten, seventy-five, and five neurons, respectively. The center layer is treated as the main layer with the most neurons, and the fewer neurons in the first and third layers can reduce the loading for training and fit with the neuron number in the input and output layers.

Figure 6 illustrates the optimized prediction results of the same structure parameters as those shown in Figure 5d–f. For the a440 dataset in Figure 6a, the predicted points do not seem fit better than in Figure 5d but still maintain the PBS's configuration. Compared to the influence of adjusting a, the influence of H is not so intense on the PBS, and therefore, increasing the complexity of the network construction rather worsens the result. On the other hand, the prediction results for the H220 and aH2 datasets shown in Figure 6b,c show significant improvement in that most of the predicted points are close to the calculated points. Although many mismatching points still exist, considering the error tolerance that naturally occurs between the simulation and the experiment, some of the mismatches are acceptable. This result also proves that the optimization method is appropriate for using a few PBSs as the training dataset. If there is a demand for a more accurate PBS prediction, increasing the number of PBSs used for training combined with the three-layer ANN may allow for a better result to be obtained.

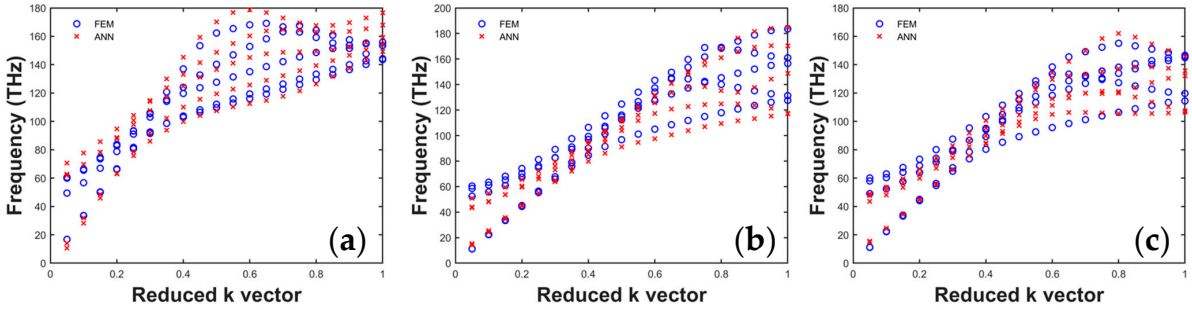

Figure 6. Prediction results for optimized ANN, (**a**) a = 440 nm, H = 550 nm using a440 dataset; (**b**) a = 660 nm, H = 220 nm using H220 dataset; and (**c**) a = 660 nm, H = 330 nm using aH2 dataset. All the PtC structures have $d = 0.4a$ and $r = 0.2a$.

4. Conclusions

This study describes the method of using a simple ANN to predict the PBS for 1-D fishbone-like PtC structures with different geometric parameters. The raw data were calculated by an FEM, and a few of them were selected as the training dataset. The influence of the geometric parameters is discussed in the beginning to show what adjusting a and H will lead to. The training dataset was first chosen from the PBSs with fixed a and H values with only the wing length d and the radius r as the variables. The prediction result of this ANN has a high accuracy for data within and outside the training dataset. Next, PBSs containing different a and H values were added to the dataset, and three types of datasets that treat only a, only H, and a/H as variables were trained. The prediction results of using the same ANN construction for testing data show terrible mismatches under an information-limited training condition. When the R value is high, the large degree of error caused by the test data is similar to that caused by overfitting. By adjusting the proportion of test data in the training data allocation ratio and adding additional hidden layers, the prediction results can be improved to an acceptable range. Due to the requirement for raw data for training being only 27 PBSs, the proposed method can significantly reduce the calculation time needed in traditional investigations of PtCs. The proposed method can

be improved by adding additional data to the training dataset depending on the desired structure parameters and has the potential to support PtC structure design.

Author Contributions: Conceptualization, F.-L.H. and Y.-C.H.; methodology, F.-L.H., C.-Y.C. and Y.-P.T.; software, F.-L.H., C.-Y.C. and Y.-P.T.; validation, F.-L.H., C.-C.C. and C.-Y.C.; formal analysis, F.-L.H., C.-C.C., C.-Y.C. and Y.-P.T.; investigation, F.-L.H., C.-C.C. and Y.-P.T.; resources, F.-L.H. and Y.-P.T.; data curation, F.-L.H. and Y.-P.T.; writing—original draft preparation, F.-L.H. and C.-C.C.; writing—review and editing, F.-L.H., C.-C.C. and Y.-P.T.; visualization, Y.-P.T. and C.-Y.C.; supervision, F.-L.H. and Y.-P.T.; project administration, F.-L.H. and Y.-P.T.; funding acquisition, F.-L.H. All authors have read and agreed to the published version of the manuscript.

Funding: This research was funded by the National Science and Technology Council (NSTC) of Taiwan, grant number 112—2221—E—018—021–.

Data Availability Statement: Dataset available on request from the authors.

Conflicts of Interest: The authors declare no conflicts of interest.

References

1. Anopchenko, A.; Tengattini, A.; Marconi, A.; Prtljaga, N.; Ramírez, J.M.; Jambois, O.; Berencén, Y.; Navarro-Urrios, D.; Garrido, B.; Milesi, F.; et al. Bipolar pulsed excitation of erbium-doped nanosilicon light emitting diodes. *J. Appl. Phys.* **2012**, *111*, 063102. [CrossRef]
2. De Valicourt, G.; Levaufre, G.; Pointurier, Y.; Le Liepvre, A.; Antona, J.C.; Jany, C.; Accard, A.; Lelarge, F.; Make, D.; Duan, G.-H. Direct modulation of hybrid-integrated InP/Si transmitters for short and long reach access network. *J. Lightw. Technol.* **2015**, *33*, 1608–1616. [CrossRef]
3. Ovvyan, A.P.; Li, M.K.; Gehring, H.; Beutel, F.; Kumar, S.; Hennrich, F.; Wei, L.; Chen, Y.; Pyatkov, F.; Krupke, R.; et al. An electroluminescent and tunable cavity-enhanced carbon-nanotube-emitter in the telecom band. *Nat. Commun.* **2023**, *14*, 3933. [CrossRef] [PubMed]
4. Tang, M.; Chen, S.; Wu, J.; Jiang, Q.; Dorogan, V.G.; Benamara, M.; Mazur, Y.I.; Salamo, G.J.; Seeds, A.; Liu, H. 1.3-mum InAs/GaAs quantum-dot lasers monolithically grown on Si substrates using InAlAs/GaAs dislocation filter layers. *Opt. Express* **2014**, *22*, 11528–11535. [CrossRef]
5. Zhang, Y.; Zhong, K.; Zhou, X.; Tsang, H.K. Broadband high-Q multimode silicon concentric racetrack resonators for widely tunable Raman lasers. *Nat. Commun.* **2022**, *13*, 3534. [CrossRef] [PubMed]
6. Dong, B.; Luo, X.; Zhu, S.; Li, M.; Hasan, D.; Zhang, L.; Chua, S.J.; Wei, J.; Chang, Y.; Lo, G.Q.; et al. Aluminum nitride on insulator (AlNOI) platform for mid-infrared photonics. *Opt. Lett.* **2019**, *44*, 73–76. [CrossRef] [PubMed]
7. Li, B.; Ho, C.P.; Lee, C. Tunable autler–townes splitting observation in coupled whispering gallery mode resonators. *IEEE Photonics J.* **2016**, *8*, 1–10. [CrossRef]
8. Sun, F.; Dong, B.; Wei, J.; Ma, Y.; Tian, H.; Lee, C. Demonstration of mid-infrared slow light one-dimensional photonic crystal ring resonator with high-order photonic bandgap. *Opt. Express* **2020**, *28*, 30736–30747. [CrossRef] [PubMed]
9. Wang, X.; Shi, W.; Yun, H.; Grist, S.; Jaeger, N.A.F.; Chrostowski, L. Narrow-band waveguide Bragg gratings on SOI wafers with CMOS-compatible fabrication process. *Opt. Express* **2012**, *20*, 15547. [CrossRef]
10. Wei, J.; Sun, F.; Dong, B.; Ma, Y.; Chang, Y.; Tian, H.; Lee, C. Deterministic aperiodic photonic crystal nanobeam supporting adjustable multiple mode-matched resonances. *Opt. Lett.* **2018**, *43*, 5407–5410. [CrossRef]
11. Chen, Y.; Li, H.; Li, M. Flexible and tunable silicon photonic circuits on plastic substrates. *Sci. Rep.* **2012**, *2*, 622. [CrossRef] [PubMed]
12. Leo Tsui, H.C.; Alsalman, O.; Mao, B.; Alodhayb, A.; Albrithen, H.; Knights, A.P.; Halsall, M.P.; Crowe, I.F. Graphene oxide integrated silicon photonics for detection of vapour phase volatile organic compounds. *Sci. Rep.* **2020**, *10*, 9592. [CrossRef] [PubMed]
13. Li, W.; Wang, Z.; Feng, C.; Li, Q.; Yu, H. High sensitivity all-optical acoustic pressure sensor based on resonant micro-opto-mechanical cantilever with integrated rib waveguide. *Sens. Actuators A Phys.* **2019**, *285*, 300–307. [CrossRef]
14. Zhao, X.; Tsai, J.M.; Cai, H.; Ji, X.M.; Zhou, J.; Bao, M.H.; Huang, Y.P.; Kwong, D.L.; Liu, A.Q. A nano-opto-mechanical pressure sensor via ring resonator. *Opt. Express* **2012**, *20*, 8535. [CrossRef] [PubMed]
15. Zuo, Y.; Gao, Y.; Qin, S.; Wang, Z.; Zhou, D.; Li, Z.; Yu, Y.; Shao, M.; Zhang, X. Broadband multi-wavelength optical sensing based on photothermal effect of 2D MXene films. *Nanophotonics* **2020**, *9*, 123–131. [CrossRef]
16. Berger, V. From photonic band gaps to refractive index engineering. *Opt. Mat.* **1999**, *11*, 131–142. [CrossRef]
17. Yablonovitch, E. Photonic band-gap structures. *J. Opt. Soc. Am. B* **1993**, *10*, 283. [CrossRef]
18. Yablonovitch, E.; Gmitter, T.J. Photonic band structure: The face-centered-cubic case. *Phys. Rev. Lett.* **1989**, *63*, 1950–1953. [CrossRef]
19. She, Y.; Liu, D.; Li, J.; Yao, M.; Zheng, Y.; Wu, F. Tunable wide-angle high-efficiency polarization selectivity based on a one-dimensional photonic crystal containing elliptical metamaterials. *Phys. Lett. A* **2024**, *494*, 129299. [CrossRef]

20. Wu, F.; Lu, G.; Guo, Z.; Jiang, H.; Xue, C.; Zheng, M.; Chen, C.; Du, G.; Chen, H. Redshift gaps in one-dimensional photonic crystals containing hyperbolic metamaterials. *Phys. Rev. Appl.* **2018**, *10*, 064022. [CrossRef]
21. Cubukcu, E.; Aydin, K.; Ozbay, E.; Foteinopoulou, S.; Soukoulis, C.M. Negative refraction by photonic crystals. *Nature* **2003**, *423*, 604–605. [CrossRef]
22. Notomi, M. Negative refraction in photonic crystals. *Opt. Quant. Electron* **2002**, *34*, 133–143. [CrossRef]
23. Vasconcelos, M.S.; Mauriz, P.W.; De Medeiros, F.F.; Albuquerque, E.L. Photonic band gaps in quasiperiodic photonic crystals with negative refractive index. *Phys. Rev. B* **2007**, *76*, 165117. [CrossRef]
24. Baba, T. Slow light in photonic crystals. *Nat. Photonics* **2008**, *2*, 465–473. [CrossRef]
25. Chung, C.-J.; Xu, X.; Wang, G.; Pan, Z.; Chen, R.T. On-chip optical true time delay lines featuring one-dimensional fishbone photonic crystal waveguide. *Appl. Phys. Lett.* **2018**, *112*, 071104. [CrossRef]
26. Soljačić, M.; Johnson, S.G. Photonic-crystal slow-light enhancement of nonlinear phase sensitivity. *J. Opt. Soc. Am. B* **2002**, *19*, 2052–2059. [CrossRef]
27. He, J.; Jin, Y.; Hong, Z.; He, S. Slow light in a dielectric waveguide with negative-refractive-index photonic crystal cladding. *Opt. Express* **2008**, *16*, 11077–11082. [CrossRef] [PubMed]
28. Headland, D.; Fujita, M.; Nagatsuma, T. Bragg-mirror suppression for enhanced bandwidth in terahertz photonic crystal waveguides. *IEEE J. Sel. Top. Quant.* **2020**, *26*, 4900109. [CrossRef]
29. Wang, Q.; Ouyang, Z.; Tao, K.; Lin, M.; Ruan, S. T-shaped optical circulator based on coupled magneto-optical rods and a side-coupled cavity in a square-lattice photonic crystal. *Phys. Lett. A* **2012**, *376*, 646–649. [CrossRef]
30. Altug, H.; Vučkovic, J. Two-dimensional coupled photonic crystal resonator arrays. *Appl. Phys. Lett.* **2004**, *84*, 161–163. [CrossRef]
31. Yu, S.P.; Lucas, E.; Zang, J.; Papp, S.B. A continuum of bright and dark-pulse states in a photonic-crystal resonator. *Nat. Commun.* **2022**, *13*, 3134. [CrossRef] [PubMed]
32. Mandal, S.; Serey, X.; Erickson, D. Nanomanipulation using silicon photonic crystal resonators. *Nano Lett.* **2010**, *10*, 99–104. [CrossRef] [PubMed]
33. Baldycheva, A.; Tolmachev, V.A.; Perova, T.S.; Zharova, Y.A.; Astrova, E.V.; Berwick, K. Silicon photonic crystal filter with ultrawide passband characteristics. *Opt. Lett.* **2011**, *36*, 1854–1856. [CrossRef] [PubMed]
34. Nemec, H.N.; Kužel, P.; Duvillaret, L.; Pashkin, A.; Dressel, M.; Sebastian, M.T. Highly tunable photonic crystal filter for the terahertz range. *Opt. Lett.* **2005**, *30*, 549–551.
35. Maigyte, L.; Staliunas, K. Spatial filtering with photonic crystals. *Appl. Phys. Rev.* **2015**, *2*, 011102. [CrossRef]
36. Deng, C.-S.; Gao, Y.-S.; Wu, X.-Z.; Li, M.-J.; Zhong, J.-X. Ultrahigh-Q TE/TM dual-polarized photonic crystal holey fishbone-like nanobeam cavities. *Europhys. Lett.* **2014**, *108*, 54006. [CrossRef]
37. Froch, J.E.; Kim, S.; Stewart, C.; Xu, X.; Du, Z.; Lockrey, M.; Toth, M.; Aharonovich, I. Photonic nanobeam cavities with nanopockets for efficient integration of fluorescent nanoparticles. *Nano Lett.* **2020**, *20*, 2784–2790. [CrossRef] [PubMed]
38. Lu, T.-W.; Lin, P.-T.; Lee, P.-T. One-dimensional photonic crystal fishbone hybrid nanocavity with nanoposts. *Appl. Phys. Lett.* **2014**, *104*. [CrossRef]
39. Hsiao, F.-L.; Tsai, Y.-P.; Chang, W.-S.; Chiu, C.-C.; Lin, B.-S.; Chiang, C.-T. Photo-elastic enhanced optomechanic one dimensional phoxonic fishbone nanobeam. *Crystals* **2022**, *12*, 191107. [CrossRef]
40. Navarro-Urrios, D.; Colombano, M.F.; Arregui, G.; Madiot, G.; Pitanti, A.; Griol, A.; Makkonen, T.; Ahopelto, J.; Sotomayor-Torres, C.M.; Martinez, A. Room-temperature silicon platform for GHz-frequency nanoelectro-opto-mechanical systems. *ACS Photonics* **2022**, *9*, 413–419. [CrossRef]
41. Tsai, Y.-P.; Jhan, J.-J.; Lin, B.S.; Hsiao, F.L. Acousto-optic coupling in 1-D phoxonic potential well nanobeam cavity using slow modes. *Int. J. Optomechatronics* **2023**, *17*, 2199804. [CrossRef]
42. Abiodun, O.I.; Kiru, M.U.; Jantan, A.; Omolara, A.E.; Dada, K.V.; Umar, A.M.; Linus, O.U.; Arshad, H.; Kazaure, A.A.; Gana, U. Comprehensive review of artificial neural network applications to pattern recognition. *IEEE Access* **2019**, *7*, 158820–158846. [CrossRef]
43. Prashanth, D.S.; Mehta, R.V.K.; Sharma, N. Classification of handwritten Devanagari number—An analysis of pattern recognition tool using neural network and CNN. *Procedia Comput. Sci.* **2020**, *167*, 2445–2457. [CrossRef]
44. Wu, H.; Huang, Q.; Wang, D.; Gao, L. A CNN-SVM combined model for pattern recognition of knee motion using mechanomyography signals. *J. Electromyogr. Kinesiol.* **2018**, *42*, 136–142. [CrossRef]
45. Qu, Y.; Zhu, H.; Shen, Y.; Zhang, J.; Tao, C.; Ghosh, P.; Qiu, M. Inverse design of an integrated-nanophotonics optical neural network. *Sci. Bull.* **2020**, *65*, 1177–1183. [CrossRef] [PubMed]
46. Wang, N.; Yan, W.; Qu, Y.; Ma, S.; Li, S.Z.; Qiu, M. Intelligent designs in nanophotonics: From optimization towards inverse creation. *PhotoniX* **2021**, *2*, 22. [CrossRef]
47. Dong, B.; Zhang, Z.; Shi, Q.; Wei, J.; Ma, Y.; Xiao, Z.; Lee, C. Biometrics-protected optical communication enabled by deep learning–enhanced triboelectric/photonic synergistic interface. *Sci. Adv.* **2022**, *8*, eabl9874. [CrossRef]

Disclaimer/Publisher's Note: The statements, opinions and data contained in all publications are solely those of the individual author(s) and contributor(s) and not of MDPI and/or the editor(s). MDPI and/or the editor(s) disclaim responsibility for any injury to people or property resulting from any ideas, methods, instructions or products referred to in the content.